

---

# PROJECTION BASED MODEL REDUCTION FOR THE IMMERSED BOUNDARY METHOD

---

A PREPRINT

**Yushuang Luo**

Department of Mathematics  
The Pennsylvania State University, University Park, PA 16802, USA  
yz155@psu.edu

**Xiantao Li**

Department of Mathematics,  
The Pennsylvania State University, University Park, PA 16802, USA  
xx112@psu.edu

**Wenrui Hao**

Department of Mathematics  
The Pennsylvania State University, University Park, PA 16802, USA  
wxh64@psu.edu

November 17, 2021

## ABSTRACT

Fluid-structure interactions are central to many bio-molecular processes, and they impose a great challenge for computational and modeling methods. In this paper, we consider the immersed boundary method (IBM) for biofluid systems, and to alleviate the computational cost, we apply reduced-order techniques to eliminate the degrees of freedom associated with the large number of fluid variables. We show how reduced models can be derived using Petrov-Galerkin projection and subspaces that maintain the incompressibility condition. More importantly, the reduced-order model is shown to preserve the Lyapunov stability. We also address the practical issue of computing coefficient matrices in the reduced-order model using an interpolation technique. The efficiency and robustness of the proposed formulation are examined with test examples from various applications.

**Keywords** model reduction, fluid-structure interaction, immersed boundary method

## 1 Introduction

Biofluid dynamics, the study of cellular movement in biological fluid flow, is essential for understanding how the cellular behavior changes within living tissue [1]. With the rapid development of scientific computing, mathematical modeling and numerical simulations have become an indispensable approach for studying biofluid dynamics. Specifically, the interaction between cell structures and the surrounding fluid flow is of the major interest. Mathematically speaking, this belongs to a large class of problems known as the fluid-structure interaction (FSI) problem, often described by coupling the incompressible Navier–Stokes equations with solid equations. A variety of computational modeling techniques have been developed for FSIs, and they have been successfully implemented in studying (among many other applications) biology and biomedical diseases [2, 3, 4, 5, 6, 7, 8, 9]. In order to numerically solve the FSI problem, several numerical methods have been developed to represent/track the interface movement explicitly such as the boundary element method (BEM) [10, 11, 12], IBM [13, 14, 15], immersed interface method (IIM) [16, 17], fictitious domain method (FDM) [18, 19], and front tracking method (FTM) [20, 21]. Another alternative approach to solve the FSI problem is to capture the interface dynamics by evolving a scalar function defined on the whole domain,

e.g. the level set method [22], phase field method [23], and the implicit boundary integral method [24]. However, direct simulations based on these methods tend to be time-consuming and computationally expensive for the prediction and analysis of long-term dynamics although the short-term prediction is certainly feasible. Moreover, only the structure dynamics are used to validate the model by biological data. In practice, there are many important scenarios where the cell structure is immersed in a large fluid environment, and simulating the entire system becomes computationally challenging.

The purpose of this paper is to explore an alternative to reduce the computational cost using reduced-order techniques, which have been applied to a wide variety of problems in science and engineering [25, 26, 27, 28]. Reduced-order modeling is concerned with large-dimensional dynamical systems with low-dimensional input and output, and the main objective is to construct reduced models that can approximate the mapping from the input to the output. For the present problem, the dynamics of the fluid variables, together with the force exerted from the structure as the input and the fluid velocity as the output to determine the local velocity of the structure, will be formulated as a reduced-order problem. As proof of concept, we utilize the IBM model [13] to solve the FSI problem in this paper, but the extension to other methods is also possible. Our starting point is a semi-discrete representation of the IBM model, so that the dynamics can be expressed as coupled ODEs, which can be considered in the reduced-order modeling framework. Then we derive the effective mapping from the structure force to the local velocity, which completely eliminates the fluid variables.

To construct specific reduced models that do not involve the fluid dynamics explicitly, we first construct subspaces that preserve the incompressibility condition, followed by a Petrov-Galerkin projection. We show that the choice of the subspaces ensures certain interpolation conditions on the underlying transfer function. An important departure from standard reduced-order problems is that in IBM, the structure is also evolving continuously. As a result, the subspaces are varying in time. This leads to the outstanding issues that the coefficients of the reduced models need to be updated frequently. To circumvent this issue, we observed the connection between the coefficient matrices and the Green's function of the Laplace equation. More specifically, the entries of the coefficient matrices are tied to the nodal points on the structure. When the two points are far apart, the corresponding entry can be well approximated by the Green's function. On the other hand, for points that are within some cut-off distance, the computation can be done in advance, and then in the simulation, those entries can be computed by interpolation. We show that such a strategy avoids repetitive computation of those coefficient matrices and it can speed up the computation considerably.

The remaining part of the paper is organized as follows: in Section 2, we introduce the full-order model (FOM) in the IBM setup; in Section 3, we formulate the reduced-order model (ROM); several numerical examples are used to compare both full-order and reduced-order models in Section 4; then the conclusion is drawn in Section 5.

## 2 Full-order Model

In this section we briefly review the mathematical formulation of the IBM and derive its semi-discrete representation as the full-order model (FOM).

### 2.1 Mathematical formulation of the IBM

The IBM is intended for the computer simulation of FSI, especially in biological fluid dynamics. It is mathematically defined by a set of differential equations involving a mixture of Eulerian and Lagrangian descriptions, linked by the Dirac delta function. The dynamics of the fluid is described by the velocity  $\mathbf{u}(\mathbf{x}, t)$  and pressure  $p(\mathbf{x}, t)$  on an Eulerian coordinate. The immersed structures, on the other hand, are handled in a Lagrangian coordinate, typically as a parametric curve  $X(\mathbf{s}, t)$  but can be extended to multiple dimensions to model surfaces or three-dimensional solids. Specifically,  $X(\mathbf{s}, t)$  represents the position at time  $t$  in Cartesian coordinates of the structure point labeled  $\mathbf{s}$ . Assuming constant density, the time-dependent Stokes equation is used to model the incompressible flow

$$\rho \frac{\partial \mathbf{u}}{\partial t} = -\nabla p + \mu \nabla^2 \mathbf{u} + \mathbf{f}, \quad (1)$$

$$\nabla \cdot \mathbf{u} = 0, \quad (2)$$

where  $\rho$  and  $\mu$  are the fluid density and viscosity, respectively. The body force  $\mathbf{f}$  exerted by the structure on the fluid is defined as

$$\mathbf{f}(\mathbf{x}, t) = \int_{\Gamma} \mathbf{F}(\mathbf{s}, t) \delta(\mathbf{x} - \mathbf{X}(\mathbf{s}, t)) d\mathbf{s}, \quad (3)$$

where  $\Gamma$  represents the structure domain and  $\delta(\mathbf{x})$  is the Dirac delta function. In addition,  $\mathbf{F}(\mathbf{s}, t)$  denotes the force density on the IB surface defined as

$$\mathbf{F}(\mathbf{s}, t) = \mathcal{F}[\mathbf{X}(\mathbf{s}, t)], \quad (4)$$

where  $\mathcal{F}$  is a functional of the IBM configuration. Spring forces, bending resistance or any other type of behavior (area and volume conservation constraints) can be built into this functional to embody the physics of the immersed structure for different circumstances [19, 29]. We give detailed description of the force density in section 4 for different numerical examples.

Assuming an over-damped structure, the immersed boundary must move with the local fluid velocity:

$$\frac{\partial \mathbf{X}(\mathbf{s}, t)}{\partial t} = \mathbf{u}(\mathbf{X}(\mathbf{s}, t), t) = \int_{\Omega} \mathbf{u}(\mathbf{x}, t) \delta(\mathbf{x} - \mathbf{X}(\mathbf{s}, t)) d\mathbf{x}, \quad (5)$$

where  $\Omega$  represents the fluid domain. This last equation is nothing other than the no-slip condition written as a delta function convolution.

## 2.2 The semi-discrete equations

To derive a semi-discrete representation of the IBM, we use the finite difference discretization [13]. Similarly, other numerical methods can also be applied to the discretization of the IBM, e.g. the finite element method [30], and the finite volume method [31], in which the state space consists of nodal values.

In this work, fluid variables are discretized on a uniform staggered Eulerian grid, denoted  $\Omega_h$ . The Eulerian grid points are of the form  $\mathbf{x} = \mathbf{j}h$ , where  $\mathbf{j} = (j_1, j_2, j_3)$  is a 3-vector with integer components and  $h$  is the Eulerian grid size. The structures are discretized on an independent Lagrangian grid, denoted by  $\Gamma_h$ . The Lagrangian grid is a set of  $\mathbf{s} = (s_1, s_2, s_3)$  of the form  $(k_1\Delta s_1, k_2\Delta s_2, k_3\Delta s_3)$ , where  $\mathbf{k} = (k_1, k_2, k_3)$  has integer components. The following restriction is imposed to avoid leak,

$$|\mathbf{X}(s_1 + \Delta s_1, s_2, s_3, t) - \mathbf{X}(s_1, s_2, s_3, t)| < \frac{h}{2},$$

for all  $(s_1, s_2, s_3, t)$ , and similarly for  $\Delta s_2, \Delta s_3$ .

First, the semi-discrete equations for (1)-(2) form a system of linear differential-algebraic equations (DAEs)

$$\begin{aligned} \rho \dot{\mathbf{u}}_h(t) &= -N\mathbf{p}_h(t) + \mu G\mathbf{u}_h(t) + \mathbf{f}_h(t), \\ 0 &= M\mathbf{u}_h(t), \end{aligned} \quad (6)$$

where

$$\mathbf{u}_h(t) = \begin{bmatrix} \vdots \\ u_h(\mathbf{x}, t) \\ \vdots \end{bmatrix} \in \mathbb{R}^{n_u}, \quad \mathbf{p}_h(t) = \begin{bmatrix} \vdots \\ p_h(\mathbf{x}, t) \\ \vdots \end{bmatrix} \in \mathbb{R}^{n_p}, \quad \mathbf{f}_h(t) = \begin{bmatrix} \vdots \\ f_h(\mathbf{x}, t) \\ \vdots \end{bmatrix} \in \mathbb{R}^{n_u}, \quad \forall \mathbf{x} \in \Omega_h,$$

are vectors of discrete velocity field, pressure and body force, respectively.  $G \in \mathbb{R}^{n_u, n_u}$  is the discrete Laplace operator. Matrices  $N \in \mathbb{R}^{n_u, n_p}$  and  $M \in \mathbb{R}^{n_p, n_u}$  are the discrete gradient and divergence operators.

Second, the integrals in (3) and (5) are replaced by sums over the appropriate grid points. Assuming 3D structures and 3D flow, we have

$$f_h(\mathbf{x}, t) = \sum_{\mathbf{s} \in \Gamma_h} F_h(\mathbf{s}, t) \delta_r(\mathbf{x} - X_h(\mathbf{s}, t)) \Delta s_1 \Delta s_2 \Delta s_3 \quad \forall \mathbf{x} \in \Omega_h, \quad (7)$$

$$\dot{X}_h(\mathbf{s}, t) = \sum_{\mathbf{x} \in \Omega_h} u_h(\mathbf{x}, t) \delta_r(\mathbf{x} - X_h(\mathbf{s}, t)) h^3 \quad \forall \mathbf{s} \in \Gamma_h, \quad (8)$$

where  $F_h(\mathbf{s}, t)$  is the discrete Lagrangian force density associated with the structure point  $\mathbf{s}$ , obtained by discretizing (4). In addition, a function  $\delta_r(\mathbf{x})$  that is nonsingular for each  $r$  but approaches  $\delta(\mathbf{x})$  as  $r \rightarrow 0$  is needed. There are many ways to construct such  $\delta_r$ . We choose a radially symmetric function with compact support as follows [32],

$$\delta_r(\mathbf{x}) = \begin{cases} C_r \left[ 1 + \frac{|\mathbf{x}|^2}{r^3} (2|\mathbf{x}| - 3r) \right] & |\mathbf{x}| \leq r, \\ 0 & |\mathbf{x}| > r, \end{cases}$$

where the normalizing constant  $C_r$  depends on  $r$  and the space dimension. In particular,

$$C_r = \begin{cases} \frac{10}{3\pi}r^{-2}, & \text{in 2D,} \\ \frac{15}{4\pi}r^{-3}, & \text{in 3D.} \end{cases}$$

For computational efficiency, we choose  $r = 2h$  in all our numerical experiments, as suggested for IBM [13].

Meanwhile, equations (7) and (8) can be put into matrix-vector form:

$$\begin{aligned} \mathbf{f}_h(t) &= B\mathbf{F}_h(t), \\ \dot{\mathbf{X}}_h(t) &= h^3 B^T \mathbf{u}_h(t), \end{aligned} \tag{9}$$

where

$$\mathbf{F}_h(t) = \begin{bmatrix} \vdots \\ F_h(\mathbf{s}, t) \Delta s_1 \Delta s_2 \Delta s_3 \\ \vdots \end{bmatrix} \in \mathbb{R}^{n_s}, \quad \mathbf{X}_h(t) = \begin{bmatrix} \vdots \\ X_h(\mathbf{s}, t) \\ \vdots \end{bmatrix} \in \mathbb{R}^{n_s}, \quad \forall \mathbf{s} \in \Gamma_h,$$

are the discrete representations of the structure position and the Lagrangian force density. Using natural arrangement of the fluid variables,  $B \in \mathbb{R}^{n_u, n_s}$  can be constructed as a block matrix

$$B = \begin{bmatrix} B_1 & 0 \\ 0 & B_2 \end{bmatrix} \text{ in 2D, or } B = \begin{bmatrix} B_1 & 0 & 0 \\ 0 & B_2 & 0 \\ 0 & 0 & B_3 \end{bmatrix} \text{ in 3D.}$$

Here the blocks  $B_i$ 's are not identical because a staggered grid is used instead of a collocated grid. A column of each block consists of evaluations of  $\delta_r(\mathbf{x} - X(\mathbf{s}, t))$  for a fixed  $X(\mathbf{s}, t)$  on grid points  $\mathbf{x}$  that store one component of the fluid velocity variables. For example, the  $i, j$ -entry of  $B_1$  is  $\delta_r(\mathbf{x}_i - X(\mathbf{s}_j, t))$ , where  $\mathbf{x}_i$  is the grid point that stores the  $i$ th fluid velocity in the  $x$ -direction. We also point out that  $B$  is time dependent due to its dependence on  $\mathbf{X}_h(t)$ .

Lastly, by substituting (9) into (6) for  $\mathbf{f}_h(t)$ , we get the following DAE system which we shall refer to as the FOM

$$\rho \dot{\mathbf{u}}_h(t) = -N\mathbf{p}_h(t) + \mu G\mathbf{u}_h(t) + B\mathbf{F}_h(t), \tag{10}$$

$$0 = M\mathbf{u}_h(t), \tag{11}$$

$$\dot{\mathbf{X}}_h(t) = h^3 B^T \mathbf{u}_h(t). \tag{12}$$

In general, the number of structure variables is much less than the number of fluid variables, i.e.  $n_s \ll n_u$ . In fact,  $\delta_r$  having compact support means only a small fraction of the Eulerian grid points are directly interacting with the structure. If one is only interested in the motion of the structure, i.e.  $\mathbf{X}_h(t)$ , solving the system (10)-(12) becomes a reduce-order problem [33], where  $\mathbf{F}_h(t)$  is the low-dimensional input and  $\dot{\mathbf{X}}_h(t)$  is the low-dimensional output.

### 3 Reduced-order Model

To construct our ROM, we start by transforming the DAE system (10)-(12) to a coupled ODE system. Multiplying (10) by  $M$  to the left and using (11), we rewrite (10) as:

$$0 = -MN\mathbf{p}_h(t) + \mu MG\mathbf{u}_h(t) + MB\mathbf{F}_h(t).$$

Assuming  $MN$  is nonsingular, it follows that

$$\mathbf{p}_h(t) = (MN)^{-1} (\mu MG\mathbf{u}_h(t) + MB\mathbf{F}_h(t)). \tag{13}$$

Substituting (13) into (10) for  $\mathbf{p}_h(t)$ , one gets

$$\rho \dot{\mathbf{u}}_h(t) = \mu QG\mathbf{u}_h(t) + QB\mathbf{F}_h(t),$$

where

$$Q = I - N(MN)^{-1}M$$

is an oblique projection.

An ODE system is then obtained from (10),

$$\dot{\mathbf{u}}_h(t) = \frac{\mu}{\rho} QG\mathbf{u}_h(t) + \frac{1}{\rho} QB\mathbf{F}_h(t), \tag{14}$$

$$\dot{\mathbf{X}}_h(t) = h^3 B^T \mathbf{u}_h(t). \tag{15}$$

We assume  $\mathbf{u}_h(0) = \mathbf{0}$  in the rest of this section. Nonzero initial values can be handled by linear superposition

$$\mathbf{u}_h(t) = \mathbf{u}_h^{(0)}(t) + \mathbf{u}_h^{(1)}(t),$$

in which  $\mathbf{u}_h^{(0)}(0) = \mathbf{0}$  and  $\mathbf{u}_h^{(1)}(0) = \mathbf{u}_h(0)$ . Then one can decompose (14)-(15) to

$$\begin{aligned}\dot{\mathbf{u}}_h^{(0)}(t) &= \frac{\mu}{\rho} QG\mathbf{u}_h^{(0)}(t) + \frac{1}{\rho} QB\mathbf{F}_h(t), \\ \dot{\mathbf{u}}_h^{(1)}(t) &= \frac{\mu}{\rho} QG\mathbf{u}_h^{(1)}(t), \\ \dot{\mathbf{X}}_h(t) &= h^3 B^T (\mathbf{u}_h^{(0)}(t) + \mathbf{u}_h^{(1)}(t)).\end{aligned}$$

The dynamics of  $\mathbf{u}_h^{(1)}(t)$ , which has nonzero initial value, is described by a first-order linear ODE, thus can be resolved analytically.

We consider a general Galerkin projection of (14), motivated by its success in order reduction problems [33, 25]. More specifically, we seek  $\tilde{\mathbf{u}}_h(t)$  in a subspace, spanned by the columns of a matrix  $V$ , as an approximation for  $\mathbf{u}_h(t)$ , such that for any  $\mathbf{w}(t)$  in a test space, spanned by the columns of the matrix  $W$ , we have

$$\left( \dot{\tilde{\mathbf{u}}}_h(t) - \frac{\mu}{\rho} QG\tilde{\mathbf{u}}_h(t) - \frac{1}{\rho} QB\mathbf{F}_h(t), \mathbf{w}(t) \right) = 0.$$

In a matrix-vector form, the approximate solution is written as

$$\tilde{\mathbf{u}}_h(t) = V\mathbf{z}(t).$$

Then the Galerkin projection yields a reduced-order equation

$$W^T(\dot{V}\mathbf{z})(t) = \frac{\mu}{\rho} W^T QGV\mathbf{z}(t) + \frac{1}{\rho} W^T QB\mathbf{F}_h(t).$$

Thus we obtain an ROM of (14) - (15)

$$\dot{\mathbf{z}}(t) = M_0^{-1} M_1 \mathbf{z}(t) + M_0^{-1} M_2 \mathbf{F}_h(t), \quad (16)$$

$$\dot{\mathbf{X}}_h(t) \approx h^3 B^T V \mathbf{z}(t), \quad (17)$$

where

$$M_0 = W^T V, \quad M_1 = \frac{\mu}{\rho} W^T QGV - W^T \dot{V}, \quad M_2 = \frac{1}{\rho} W^T QB,$$

assuming  $M_0$  is nonsingular. The computation of the coefficient matrices  $M_0$ ,  $M_1$  and  $M_2$  depends on  $V$  and  $W$ . In the rest of this section we first discuss our choice for subspaces  $V$ ,  $W$  and their properties. Then we demonstrate how interpolation helps accelerate the computation of the coefficients by exploiting the connection between matrix entries and the Green's function.

### 3.1 Subspace Selection

We propose the following choice of  $V$  and  $W$ ,

$$V = QB, \quad W = B.$$

For later reference, note that both subspaces vary in time. The resulting coefficient matrices are given by

$$M_0 = B^T QB, \quad M_1 = \frac{\mu}{\rho} B^T QGQB - B^T Q\dot{B}, \quad M_2 = \frac{1}{\rho} B^T QB = \frac{1}{\rho} M_0. \quad (18)$$

In principle, one can extend these subspaces using Krylov subspaces, followed by Lanczos orthogonalization algorithms [25, 33, 34]. But we will see from the numerical tests, the current subspaces are sufficient to capture the dynamics of the structure.

### 3.1.1 Transfer function approximation

Solving the full model (14) - (15) for  $\dot{\mathbf{X}}_h(t)$  analytically, we obtain

$$\dot{\mathbf{X}}_h(t) = \int_0^t h(t - \tau) \mathbf{F}_h(\tau) d\tau,$$

where the transfer function  $h(t)$  can be expressed in terms of a matrix exponential,

$$h(t) = \frac{h^3}{\rho} B^T \exp\left[\frac{\mu}{\rho} t Q G\right] Q B. \quad (19)$$

A similar calculation for the reduced-order model (16) - (17) shows

$$\dot{\mathbf{X}}_h(t) \approx \int_0^t h_r(t - \tau) \mathbf{F}_h(\tau) d\tau,$$

where the transfer function  $h_{red}(t)$  of the reduced-order model is

$$\begin{aligned} h_{red}(t) &= h^3 B^T V \exp[t M_0^{-1} M_1] M_0^{-1} M_2, \\ &= \frac{h^3}{\rho} B^T Q B \exp\left[t (B^T Q B)^{-1} \left(\frac{\mu}{\rho} B^T Q G Q B - B^T Q \dot{B}\right)\right]. \end{aligned} \quad (20)$$

$h_{red}(t)$  is expected to approximate  $h(t)$  in the sense that

$$\begin{aligned} h_{red}(0) &= h(0), \\ \dot{h}_{red}(0) &= \dot{h}(0). \end{aligned} \quad (21)$$

The equality (21) follows immediately from evaluating (19) and (20) at  $t = 0$ . Differentiating (19) and (20) at  $t = 0$  yields

$$\dot{h}_{red}(0) = \frac{\mu h^3}{\rho^2} B^T Q B (B^T Q B)^{-1} B^T Q G Q B = \frac{\mu h^3}{\rho^2} B^T Q G Q B = \dot{h}(0).$$

In the above calculation, we have treated  $B$  as a constant matrix. The reason is that we are only concerned with a small time interval  $[0, t]$ , typically with the size of one time step. In numerical simulations, matrix  $B$  is usually treated as constant when advancing one time step.

### 3.1.2 Enforcing incompressibility

Another essential property of the full model is incompressibility of the fluid. Recall that  $M$  is the discrete divergence operator. The approximate fluid solution,

$$\tilde{\mathbf{u}}_h(t) = V \mathbf{z}(t),$$

is incompressible if

$$M \tilde{\mathbf{u}}_h(t) = M V \mathbf{z}(t) = 0.$$

A quick calculation verifies that our choice of  $V = Q B$  satisfies this constraint

$$M V = M Q B = M (I - N (M N)^{-1} M) B = (M - M N (M N)^{-1} M) B = 0 B = 0.$$

Therefore, the incompressibility property is preserved in the ROM.

### 3.1.3 Lyapunov Stability

The ROM also preserves Lyapunov stability of the FOM with our choice of subspaces. We first show the stability of the FOM. We assume the discrete Lagrangian force density  $\mathbf{F}_h$  is given by an energy functional  $W(\mathbf{X}_h)$  of the structure configuration, i.e.,

$$\mathbf{F}_h(t) = -\nabla_{\mathbf{X}_h} W(\mathbf{X}_h(t)).$$

We also assume the discrete gradient and divergence operators satisfy

$$M = N^T,$$

such that

$$Q = I - \Sigma = I - N (N^T N)^{-1} N^T$$

is an orthogonal projection. It follows that  $Q^2 = Q$  and  $Q^T = Q$ . We now define the following Lyapunov functional for the FOM

$$V(\mathbf{u}_h(t), \mathbf{X}_h(t)) = \mathbf{u}_h(t)^T Q^+ \mathbf{u}_h(t) + \frac{1}{h^3 \rho} W(\mathbf{X}_h(t)),$$

where  $Q^+$  denotes the pseudoinverse of  $Q$ . We have  $V(\mathbf{u}_h(t), \mathbf{X}_h(t)) \geq 0$  because  $Q$  is positive semidefinite with eigenvalues 0 and 1. A direct calculation shows that

$$\begin{aligned} \dot{V}(\mathbf{u}_h(t), \mathbf{X}_h(t)) &= \mathbf{u}_h(t)^T Q^+ Q \left( \frac{\mu}{\rho} G \mathbf{u}_h(t) + \frac{1}{\rho} B \mathbf{F}_h(t) \right) - \frac{1}{\rho} \mathbf{u}_h(t)^T B \mathbf{F}_h(t) \\ &= \frac{\mu}{\rho} \mathbf{u}_h(t)^T G \mathbf{u}_h(t) \leq 0, \end{aligned}$$

since the discrete Laplace operator  $G$  is negative semidefinite. This implies Lyapunov stability of the FOM.

The Lyapunov functional for the ROM is defined as follows

$$V_r(\mathbf{X}_h(t)) = \frac{h^3}{\rho} W(\mathbf{X}_h(t)) + \frac{1}{2} \dot{\mathbf{X}}_h(t)^T (B^T Q B)^{-1} \dot{\mathbf{X}}_h(t).$$

$V_r(\mathbf{X}_h(t)) \geq 0$  holds for all  $t$  since  $B^T Q B$  is positive semidefinite.

To prove  $\dot{V}_r(\mathbf{X}_h(t)) \leq 0$ , we start by rewriting the ROM (16) - (17) as a second-order ODE of  $\mathbf{X}_h$ . Using the symmetry of  $Q$ , one has,

$$\ddot{\mathbf{X}}_h = (B^T Q \dot{B} + B^T Q G Q B) (B^T Q B)^{-1} \dot{\mathbf{X}}_h + \frac{h^3}{\rho} B^T Q B \mathbf{F}_h(\mathbf{X}_h(t)).$$

Then the following calculation shows that  $V_r$  is nonincreasing,

$$\begin{aligned} \dot{V}_r(\mathbf{X}_h(t)) &= -\frac{h^3}{\rho} \dot{\mathbf{X}}_h^T \mathbf{F}_h + \dot{\mathbf{X}}_h^T (B^T Q B)^{-1} \ddot{\mathbf{X}}_h + \frac{1}{2} \dot{\mathbf{X}}_h^T (B^T \dot{Q} B)^{-1} \dot{\mathbf{X}}_h \\ &= \dot{\mathbf{X}}_h^T (B^T Q B)^{-1} (B^T Q G Q B) (B^T Q B)^{-1} \dot{\mathbf{X}}_h - \frac{h^3}{\rho} \dot{\mathbf{X}}_h^T \mathbf{F}_h + \frac{h^3}{\rho} \dot{\mathbf{X}}_h^T \mathbf{F}_h \\ &\quad + \dot{\mathbf{X}}_h^T (B^T Q B)^{-1} (B^T Q \dot{B}) (B^T Q B)^{-1} \dot{\mathbf{X}}_h \\ &\quad - \dot{\mathbf{X}}_h^T (B^T Q B)^{-1} (B^T Q \dot{B}) (B^T Q B)^{-1} \dot{\mathbf{X}}_h \\ &= \dot{\mathbf{X}}_h^T (B^T Q B)^{-1} (B^T Q G Q B) (B^T Q B)^{-1} \dot{\mathbf{X}}_h \\ &= \mathbf{Y}^T G \mathbf{Y} \leq 0, \end{aligned}$$

where we have defined  $\mathbf{Y} := Q B (B^T Q B)^{-1} \dot{\mathbf{X}}_h$ . The last inequality holds because  $G$  is negative semidefinite.

### 3.2 Computing the coefficients using interpolation

The coefficient matrices shown in (18) are in principle time dependent. Thus they should be updated frequently during simulation. Direct matrix multiplication for this purpose is time consuming with complexity  $O(n_u^2)$ . In the rest of this section, we propose a computationally cheaper approach using interpolation to approximate the coefficients.

We first approximate  $\dot{B}$  by

$$\dot{B}(t) \approx \frac{1}{\Delta t} (B(t) - B(t - \Delta t)).$$

The matrix  $M_1$  is then approximated by

$$M_1 \approx \frac{\mu}{\rho} B(t)^T Q G Q B(t) - \frac{1}{\Delta t} B(t)^T Q B(t) + \frac{1}{\Delta t} B(t)^T Q B(t - \Delta t).$$

Together with  $M_0 = B(t)^T Q B(t)$ , the following three matrices are needed for building our ROM

$$B(t)^T Q B(t), \quad B(t)^T Q G Q B(t), \quad B(t)^T Q B(t - \Delta t).$$

Since  $Q$  and  $G$  are constant matrices, the  $i, j$ -entry of any of the above matrices at time  $t$  is determined by the  $i$ th row of  $B(t)^T$  and the  $j$ th column of  $B(t)$  (or  $B(t - dt)$ ). Recall that each column of  $B(t)$  (or row of  $B(t)^T$ ) represents

a smoothed delta function associated with a structure point. Suppose the  $i$ th column of  $B(t)^T$  is associated with the Lagrangian grid point  $X_l \in \mathbb{R}^d$  ( $d = 2, 3$ ) and the  $j$ th column of  $B(t)^T$  (or  $B(t - dt)$ ) is associated with  $X_r \in \mathbb{R}^d$ . Given prescribed function  $\delta_r$  and a fixed Eulerian grid, the  $i, j$ -entry of a coefficient matrix is uniquely determined by  $X_l$  and  $X_r$ , which can be viewed as a function from  $\mathbb{R}^{2d}$  to  $\mathbb{R}$ . It is then natural to sample such functions before simulation starts. As the simulation runs, coefficient matrices are updated by interpolation using precomputed samples. The complexity of interpolation is typically  $O(n_s^2)$ , which is much smaller than  $O(n_u^2)$ .

Next, motivated by our numerical experiments illustrated in Fig 1, we show the interpolated  $2d$ -dimensional functions of  $X_l$  and  $X_r$  can be well approximated by  $d$ -dimensional functions of  $X_l - X_r$ . Such low-dimensional approximation significantly reduces the number of samples needed for more accurate interpolation. Hence the sampling process can also be accelerated.

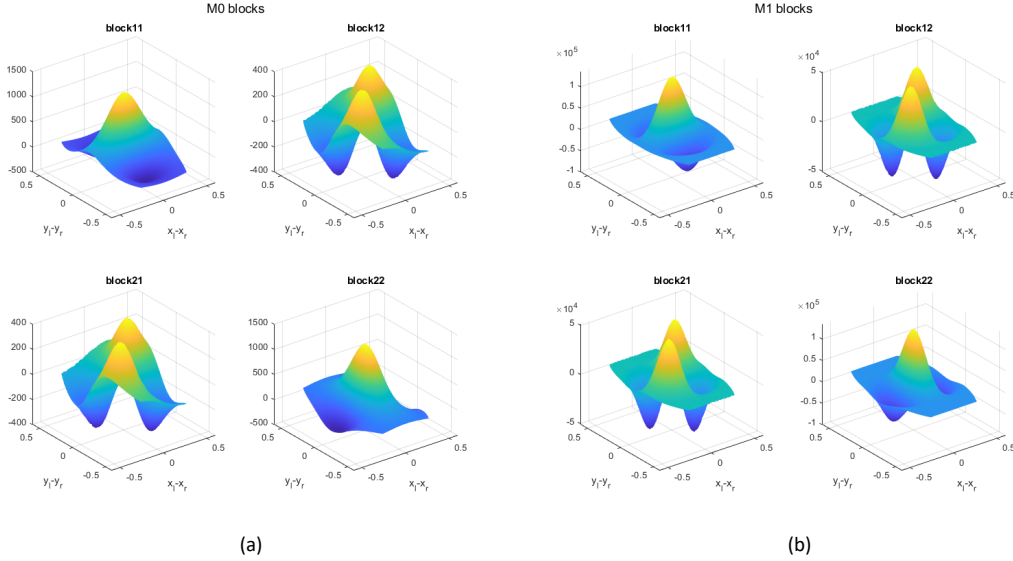


Figure 1: Surface plots of entries of (a) $M_0$  and (b) $M_1$  against  $X_l - X_r = (x_l - x_r, y_l - y_r)$  in 2D case. Both matrices are 2-by-2 block matrices where each block corresponds to a function from  $\mathbb{R}^4$  to  $\mathbb{R}$ . Large numbers of  $(X_l, X_r) = (x_l, y_l, x_r, y_r)$  pairs are sampled so that many of them correspond to the same difference  $X_l - X_r$ . Then corresponding entries of  $M_0$  and  $M_1$  blocks are plotted against  $X_l - X_r$ . In each plot, we observe a single surface, indicating no multiple values. Therefore these  $\mathbb{R}^4$  functions can be considered as functions in  $\mathbb{R}^2$  of  $X_l - X_r$ .

Here we provide justifications of this approach by making connections to the Green's functions. Recall that  $Q = I - N(MN)^{-1}M$ , where  $N$  and  $M$  are discrete gradient and divergence operators. Therefore, each entry of the matrix  $B(t)^TQB(t)$  or  $B(t)^TQB(t - \Delta t)$  is a numerical approximation of the integral

$$\begin{aligned} I_0 &= \int_{\Omega} \delta_r(\mathbf{x} - X_l)(\delta_{ij} - \partial_i \Delta^{-1} \partial_j) \delta_r(\mathbf{x} - X_r) d\mathbf{x} \\ &= \underbrace{\delta_{ij} \int_{\Omega} \delta_r(\mathbf{x} - X_l) \delta_r(\mathbf{x} - X_r) d\mathbf{x}}_{I_1} - \underbrace{\int_{\Omega} \delta_r(\mathbf{x} - X_l) \partial_i \Delta^{-1} \partial_j \delta_r(\mathbf{x} - X_r) d\mathbf{x}}_{I_2}, \end{aligned}$$

where  $i, j = 1, \dots, d$  and  $d = 2$  or  $3$ .  $\delta_{ij}$  is the Kronecker delta function.  $I_1$  only depends on  $|X_l - X_r|$  due to our choice of  $\delta_r$ . For  $I_2$ , we assume  $X_l$  and  $X_r$  are far from the boundary of  $\Omega$  so the Green's function  $G(\mathbf{x}, \mathbf{y})$  can be applied. Considering the limiting case of  $r \rightarrow 0$ , i.e.  $\delta_r \rightarrow \delta$ , we have

$$\lim_{r \rightarrow 0} I_2 = -\partial_{x_i} \partial_{y_j} G(\mathbf{x}, \mathbf{y}) \Big|_{\mathbf{x}=X_l, \mathbf{y}=X_r},$$

which depends only on  $X_l - X_r$ .



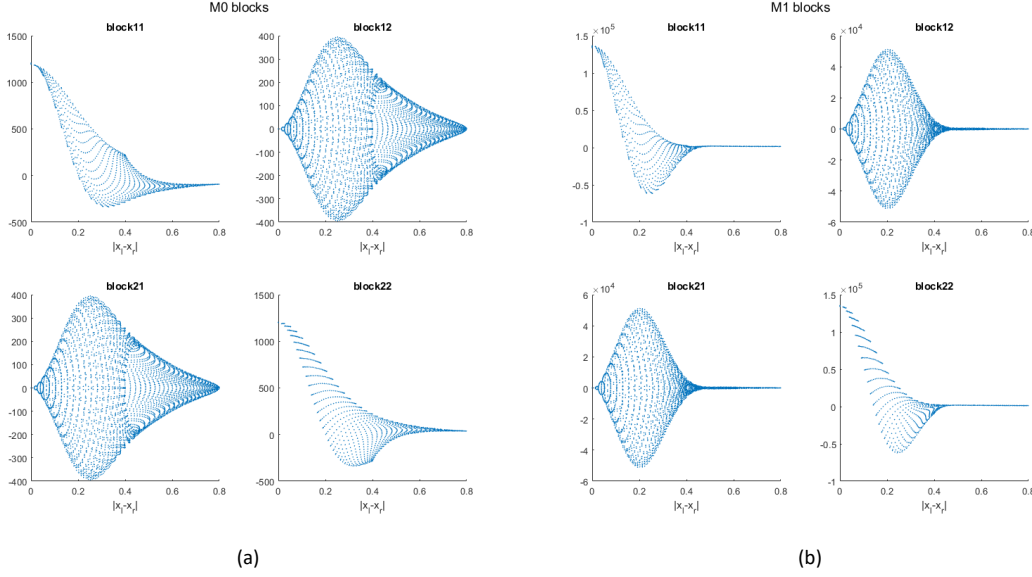


Figure 2: Scatter plots of entries of (a) $M_0$  and (b) $M_1$  against  $|X_l - X_r|$  in 2D case. Multiple values exist, indicating these  $\mathbb{R}^4$  functions may not be considered as functions in  $\mathbb{R}$  of  $|X_l - X_r|$ .

Similarly, each entry of the matrix  $B(t)^T Q G Q B(t)$  is a numerical approximation of the following integral

$$\begin{aligned}
J_0 &= \int_{\Omega} \delta_r(\mathbf{x} - X_l) (\delta_{ij} - \partial_i \Delta^{-1} \partial_j) \Delta (1 - \partial_j \Delta^{-1} \partial_j) \delta_r(\mathbf{x} - X_r) d\mathbf{x} \\
&= \underbrace{\int_{\Omega} \delta_r(\mathbf{x} - X_l) (\delta_{ij} - \partial_i \Delta^{-1} \partial_j) \Delta \delta_r(\mathbf{x} - X_r) d\mathbf{x}}_{J_1} - \underbrace{\int_{\Omega} \delta_r(\mathbf{x} - X_l) (\delta_{ij} - \partial_i \Delta^{-1} \partial_j) \Delta \partial_j \Delta^{-1} \partial_j \delta_r(\mathbf{x} - X_r) d\mathbf{x}}_{J_2} \\
&= \underbrace{\delta_{ij} \int_{\Omega} \delta_r(\mathbf{x} - X_l) \Delta \delta_r(\mathbf{x} - X_r) d\mathbf{x}}_{J_{11}} - \underbrace{\int_{\Omega} \delta_r(\mathbf{x} - X_l) \partial_i \Delta^{-1} \partial_j \Delta \delta_r(\mathbf{x} - X_r) d\mathbf{x}}_{J_{12}} \\
&\quad - \underbrace{\delta_{ij} \int_{\Omega} \delta_r(\mathbf{x} - X_l) \partial_j^2 \delta_r(\mathbf{x} - X_r) d\mathbf{x}}_{J_{21}} + \underbrace{\int_{\Omega} \delta_r(\mathbf{x} - X_l) \partial_i \Delta^{-1} \partial_j \Delta \partial_j \Delta^{-1} \partial_j \delta_r(\mathbf{x} - X_r) d\mathbf{x}}_{J_{22}},
\end{aligned}$$

where  $J_{11}$  and  $J_{21}$  depend on  $X_l - X_r$  due to our choice of  $\delta_r$ . For  $J_{12}$  and  $J_{22}$  we make the same assumptions as for  $I_2$  and consider the limiting case. We obtain similar results

$$\begin{aligned}
\lim_{r \rightarrow 0} J_{12} &= -\partial_{x_i} \partial_{y_j}^3 G(\mathbf{x}, \mathbf{y}) \Big|_{\mathbf{x}=X_l, \mathbf{y}=X_r}, \\
\lim_{r \rightarrow 0} J_{22} &= -\partial_{x_i} \Delta_y \partial_{y_j} G(\mathbf{x}, \mathbf{y}) \Big|_{\mathbf{x}=X_l, \mathbf{y}=X_r},
\end{aligned}$$

where both depends only on  $X_l - X_r$ . However, the integrals  $I_0$  and  $J_0$  may not be further reduced to functions of  $|X_l - X_r|$ , verified by our numerical experiments, see Fig 2.

## 4 Numerical results

In this section, we present three numerical examples to demonstrate the accuracy and speedup of our ROM.

### 4.1 Oscillation of an elliptical membrane

We consider the oscillations of a pressurized membrane with an initially elliptical shape. The initial configuration of the membrane is a 1D ellipse which resides in the center of a 2D stationary fluid on  $4 \times 4$  domain. The body force in

this example is generated by an elastic energy functional [13],

$$E = \int \varepsilon \left( \left| \frac{\partial \mathbf{X}}{\partial s} \right| \right) ds,$$

where  $\varepsilon$  is the local energy given by

$$\varepsilon(x) = \frac{\sigma}{2}(x - L)^2,$$

which corresponds to an elastic fiber having a "spring constant"  $\sigma$  and an equilibrium state where the elastic strain  $|\partial \mathbf{X} / \partial s| \equiv L$ . The force in (4) is then expressed as

$$F = -\nabla_X E = \sigma \frac{\partial}{\partial s} \left( \frac{\partial \mathbf{X}}{\partial s} \left( 1 - \frac{L}{|\frac{\partial \mathbf{X}}{\partial s}|} \right) \right).$$

Since the fluid in the interior of the membrane is confined, the membrane will oscillate and eventually settle into a circular state. Fig 3 shows the membrane snapshots by comparing the FOM simulation with ROM simulation at different times. The ROM simulation captures almost the same equilibrium state as the FOM. In addition, the membrane configurations are approximated accurately during the oscillation.

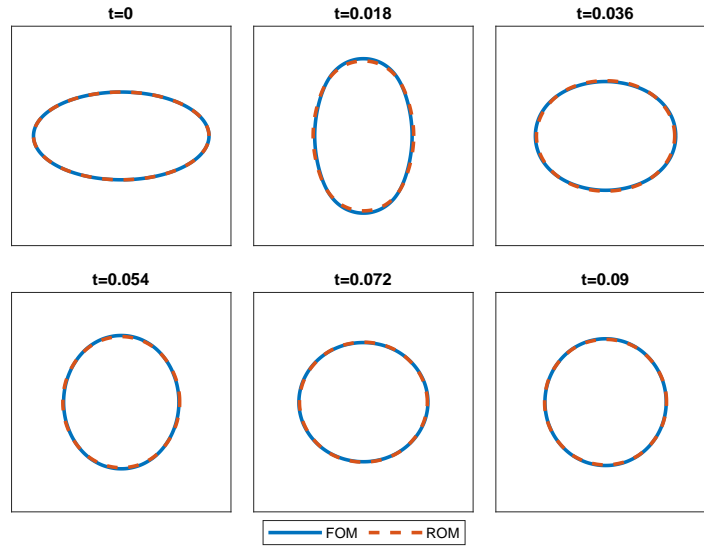


Figure 3: Profiles of an elliptical membrane at different times with comparisons between the full-order and reduced-order models.

The one-step computation time of our ROM simulations with various grid sizes is compared to the one-step FOM simulation time in Table 1. There is a clear increase in the speedup factor as the grid size decreases. With 2D flow, the order of the FOM is  $O(h^{-2})$  but the order of the ROM is  $O(h^{-1})$ .

#### 4.2 Rotation of an elliptical particle in shear flow

We study the problem of the motion of a rigid elliptical particle freely suspended in a shear flow. It has been shown that the instantaneous inclination angle  $\theta$  of the ellipse major axis with respect to the flow direction is

$$\tan(\theta) = \frac{S_2}{S_1} \tan \left( \frac{S_1 S_2}{S_1^2 + S_2^2} \dot{\gamma} t \right), \quad (22)$$

where  $\dot{\gamma}$  is the shear rate,  $S_1$  and  $S_2$  are the semi-major and minor axes of the ellipse, respectively, and  $t$  is the time variable [35].

To preserve the elliptic shape of the structure, the body force in this example is generated by a discrete bending energy. Let  $\theta_i^0$  be the initial angle between the adjacent edges with the  $i$ th Lagrangian grid point and  $\theta_i$  be the current angle. The bending energy is given by

$$E_b = \sigma_b \sum_{i=1}^{n_s} (1 - \cos(\theta_i - \theta_i^0)),$$

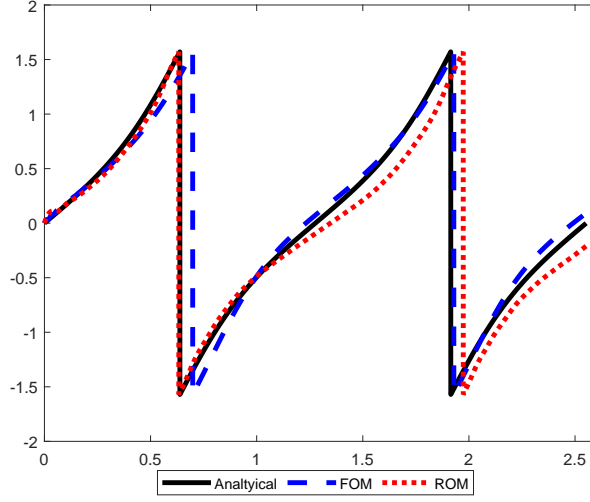


Figure 4: Ellipse rotation angles simulated by full model and reduced-order model compared with Jeffery’s orbit. The variation in angle  $\theta$  to the ellipse major axis is plotted against the time  $t$ .

where  $n_s$  is the number of Lagrangian grid points and  $\sigma_b$  is the bending coefficient [29]. In this example, we choose  $\sigma_b = 2000$  to increase stiffness. The bending force generated on each structure point is

$$\mathbf{F}_i = (F_{ix}, F_{iy}) = \left(-\frac{\partial E_b}{\partial x_i}, -\frac{\partial E_b}{\partial y_i}\right).$$

Fig 4 shows the simulated ellipse rotation rate and the analytical result (22). The rotation rate obtained by our ROM simulation is in close agreement with both the FOM simulation and the analytical solution. Table 2 shows the increase in the speedup factor as the grids become finer. Higher speedup factors are achieved for finer space grid.

### 4.3 Motion of two particles in laminar flow

We simulate the motion of two 1D membranes in 2D laminar flow. The same bending force as the previous example is applied to both membranes to prevent significant deformation. In addition, the two membranes interact with each other through a binding force and a repulsive force

$$\begin{aligned} F_{binding} &= s(d - \lambda), \\ F_{repulsion} &= ad + bd^3, \end{aligned}$$

where  $d$  is the distance between two Lagrangian nodes on different cells and  $a, b, s, \lambda$  are parameters. These forces are developed to model the biochemical interactions between flowing melanoma tumor cells and substrate adherent polymorphonuclear neutrophils [36]. Initially, the two membranes of the same shape are placed symmetrically in the laminar flow. The attraction and repulsion forces yield oscillatory trajectories for both membranes, shown in Fig 5. Table 3 shows the increase in the speedup factor as the space grid becomes finer.

## 5 Conclusion

In this paper, we develop a reduced-order modeling formulation in the FSI problem with the IBM setup and discuss the transfer function approximation. This proposed ROM formulation enforces the incompressibility condition and also preserves Lyapunov stability. An efficient interpolation technique is applied to update the time-dependent coefficient matrices. The proposed model reduction technique is applied to several biological applications, as demonstrated by the examples. Compared to other traditional methods, this new method has the following two advantages: 1) the fluid variables are not involved in the computation while they are the most time-consuming part in the traditional methods such as IBM, IIM, and FDM; 2) the structure equation is derived explicitly and does not require special discretization techniques or singular integrals that are widely used in the BEM. Recently, there have been growing interest in combining the reduced-order technique and data-driven methods. In this scenario, rather than the direct

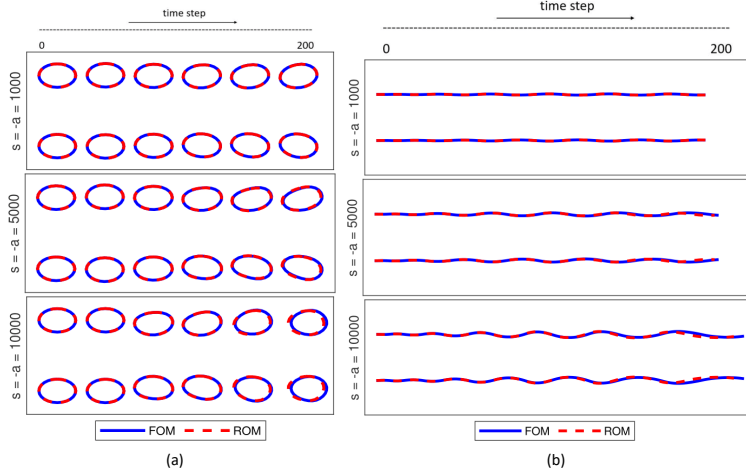


Figure 5: (a) Snapshots of two membranes at different times and (b) trajectories of membrane centers. The attraction and repulsion forces increase from top to bottom as the magnitude of  $a$  and  $s$  increases. The other two parameter,  $b$  and  $\lambda$ , are fixed for ease of comparison.

access to the FOM, one works with observations, e.g., structure conformations, in the form of time series. The problem is then reduced to inferring parameters in the ROM. This work is underway.

## Acknowledgments

This work is supported by the National Science Foundation Grant DMS-1819011 and DMS-1953120 (X. Li)

## Conflict of interest

We have no conflict of interest to report.

Table 1: Membrane oscillation: Speedup of full order model and reduced-order model.

h	Model order		CPU time		Speedup factor
	full	reduced	full	reduced	
1/6	1728	144	.0118	.0036	3.2778
1/8	3072	192	.0309	.0044	7.0227
1/12	6912	288	.1391	.007	19.871
1/16	12288	384	.3940	.0166	24.735
1/20	19200	480	.9745	.0275	35.436

Table 2: Particle rotation: Speedup of full order model and reduced-order model.

h	Model order		CPU time		Speedup factor
	full	reduced	full	reduced	
3/16	2048	32	.0214	.0017	12.5882
1/8	4608	48	.1012	.0029	34.8966
3/32	8192	64	.3065	.0057	53.7719

## References

- [1] Clement Kleinstreuer. *Biofluid Dynamics: Principles and Selected Applications*. CRC Press, 2006.
- [2] S. Canic. Blood flow through compliant vessels after endovascular repair: wall deformations induced by the discontinuous wall properties. *Computing and Visualization in Science*, 4(3):147–155, 2002.

Table 3: Two cells interaction: Speedup of full order model and reduced-order model.

h	Model order		CPU time		Speedup factor
	full	reduced	full	reduced	
3/16	4096	64	.0834	.0080	10.425
1/8	9216	96	.4272	.0148	28.8649
3/32	16384	128	1.2492	.0378	33.0476

- [3] S. Canic and D. Mirkovic. A hyperbolic system of conservation laws in modeling endovascular treatment of abdominal aortic aneurysm. In Heinrich Freistühler and Gerald Warnecke, editors, *Hyperbolic Problems: Theory, Numerics, Applications*, volume 140, pages 227–236. Birkhäuser Basel, Basel, 2001.
- [4] Huan Lei and George Em Karniadakis. Predicting the morphology of sickle red blood cells using coarse-grained models of intracellular aligned hemoglobin polymers. *Soft Matter*, 8(16):4507–4516, 2012.
- [5] Xuejin Li, Zhangli Peng, Huan Lei, Ming Dao, and George Em Karniadakis. Probing red blood cell mechanics, rheology and dynamics with a two-component multi-scale model. *Philosophical Transactions of the Royal Society A: Mathematical, Physical and Engineering Sciences*, 372(2021):20130389, 2014.
- [6] Q. Wang. A hydrodynamic theory for solutions of nonhomogeneous nematic liquid crystalline polymers of different configurations. *The Journal of Chemical Physics*, 116(20):9120–9136, 2002.
- [7] X. Yang, G. Forest, W. Mullins, and Q. Wang. Dynamic defect morphology and hydrodynamics of sheared nematic polymers in two space dimensions. *Journal of Rheology*, 53(3):589–615, 2009.
- [8] Yue Yu. Fluid-structure interaction modeling in 3d cerebral arteries and aneurysms. In Peter Wriggers and Thomas Lenarz, editors, *Biomedical Technology: Modeling, Experiments and Simulation*, pages 123–146. Springer, Cham, 2018.
- [9] J. Zhao, X. Yang, J. Shen, and Q. Wang. A decoupled energy stable scheme for a hydrodynamic phase-field model of mixtures of nematic liquid crystals and viscous fluids. *Journal of Computational Physics*, 305:539–556, 2016.
- [10] William S Hall. *The Boundary Element Method*, volume 27. Springer Netherlands, 1 edition, 1994.
- [11] Shuwang Li and Xiaofan Li. A boundary integral method for computing the dynamics of an epitaxial island. *SIAM Journal on Scientific Computing*, 33(6):3282–3302, 2011.
- [12] Gordon C Everstine and Francis M Henderson. Coupled finite element/boundary element approach for fluid-structure interaction. *The Journal of the Acoustical Society of America*, 87(5):1938–1947, 1990.
- [13] Charles S Peskin. The immersed boundary method. *Acta numerica*, 11:479–517, 2002.
- [14] Ming-Chih Lai and Charles S Peskin. An immersed boundary method with formal second-order accuracy and reduced numerical viscosity. *Journal of Computational Physics*, 160(2):705–719, 2000.
- [15] Paul J. Atzberger, Peter R. Kramer, and Charles S. Peskin. A stochastic immersed boundary method for fluid-structure dynamics at microscopic length scales. *Journal of Computational Physics*, 224(2):1255–1292, June 2007.
- [16] Randall J Leveque and Zhilin Li. The immersed interface method for elliptic equations with discontinuous coefficients and singular sources. *SIAM Journal on Numerical Analysis*, 31(4):1019–1044, 1994.
- [17] Fotis Sotiropoulos and Xiaolei Yang. Immersed boundary methods for simulating fluid-structure interaction. *Progress in Aerospace Sciences*, 65:1–21, 2014.
- [18] Roland Glowinski, Tsorng-Whay Pan, and Jacques Periaux. A fictitious domain method for dirichlet problem and applications. *Computer Methods in Applied Mechanics and Engineering*, 111(3-4):283–303, 1994.
- [19] Wenrui Hao, Zhiliang Xu, Chun Liu, and Guang Lin. A fictitious domain method with a hybrid cell model for simulating motion of cells in fluid flow. *Journal of Computational Physics*, 280:345–362, 2015.
- [20] Grétar Tryggvason, Bernard Bunner, Asghar Esmaeeli, Damir Juric, N Al-Rawahi, W Tauber, J Han, S Nas, and Y-J Jan. A front-tracking method for the computations of multiphase flow. *Journal of Computational Physics*, 169(2):708–759, 2001.
- [21] James Glimm, Xiaolin Li, Yingjie Liu, Zhiliang Xu, and Ning Zhao. Conservative front tracking with improved accuracy. *SIAM Journal on Numerical Analysis*, 41(5):1926–1947, 2003.
- [22] Georges-Henri Cottet and Emmanuel Maitre. A level set method for fluid-structure interactions with immersed surfaces. *Mathematical models and methods in applied sciences*, 16(03):415–438, 2006.

- [23] Qiang Du, Chun Liu, and Xiaoqiang Wang. A phase field approach in the numerical study of the elastic bending energy for vesicle membranes. *Journal of Computational Physics*, 198(2):450–468, 2004.
- [24] Catherine Kublik, Nicolay M Tanushev, and Richard Tsai. An implicit interface boundary integral method for poisson’s equation on arbitrary domains. *Journal of Computational Physics*, 247:279–311, 2013.
- [25] Zhaojun Bai. Krylov subspace techniques for reduced-order modeling of large-scale dynamical systems. *Applied Numerical Mathematics*, 43(1-2):9–44, Apr 2002.
- [26] Peter Benner, Serkan Gugercin, and Karen Willcox. A survey of projection-based model reduction methods for parametric dynamical systems. *SIAM Review*, 57(4):483–531, 2015.
- [27] S. Gugercin, A. Antoulas, and C. Beattie.  $\mathcal{H}_2$  Model Reduction for Large-Scale Linear Dynamical Systems. *SIAM Journal on Matrix Analysis and Applications*, 30(2):609–638, 2008.
- [28] Branimir Anic. *An interpolation-based approach to the weighted  $\mathcal{H}_2$  model reduction problem*. PhD thesis, Virginia Polytechnic Institute and State University, Virginia, 2008.
- [29] Igor V Pivkin and George Em Karniadakis. Accurate coarse-grained modeling of red blood cells. *Physical Review Letters*, 101(11):118105, 2008.
- [30] Daniele Boffi and Lucia Gastaldi. A finite element approach for the immersed boundary method. *Computers & Structures*, 81(8-11):491–501, 2003.
- [31] Jungwoo Kim, Dongjoo Kim, and Haecheon Choi. An immersed-boundary finite-volume method for simulations of flow in complex geometries. *Journal of Computational Physics*, 171(1):132–150, 2001.
- [32] Jerry Zhijian Yang, Xiaojie Wu, and Xiantao Li. A generalized irving–kirkwood formula for the calculation of stress in molecular dynamics models. *The Journal of Chemical Physics*, 137(13):134104, 2012.
- [33] Roland W Freund. Krylov-subspace methods for reduced-order modeling in circuit simulation. *Journal of Computational and Applied Mathematics*, 123(1-2):395–421, 2000.
- [34] Lina Ma, Xiantao Li, and Chun Liu. Coarse-graining langevin dynamics using reduced-order techniques. *Journal of Computational Physics*, 380:170–190, 2019.
- [35] George Barker Jeffery. The motion of ellipsoidal particles immersed in a viscous fluid. *Proceedings of the Royal Society of London. Series A*, 102(715):161–179, 1922.
- [36] Julie Behr, Byron Gaskin, Changliang Fu, Cheng Dong, and Robert Kunz. Localized modeling of biochemical and flow interactions during cancer cell adhesion. *PloS One*, 10(9):e0136926, 2015.